This is the accepted manuscript made available via CHORUS. The article has been published as:

Phase and structural stability in Ni-Al systems from first principles

Jon Gabriel Goiri and Anton Van der Ven

Phys. Rev. B **94**, 094111 — Published 27 September 2016

DOI: 10.1103/PhysRevB.94.094111

Phase and structural stability in Ni-Al systems from first principles

Jon Gabriel Goiri and Anton Van der Ven*
Materials Department, University of California Santa Barbara
(Dated: August 19, 2016)

We report on a comprehensive first-principles study of phase stability in the Ni-Al binary, both at zero Kelvin and at finite temperature. First-principles density functional theory calculations of the energies of enumerated orderings on FCC and the sublattices of B2 not only predict the stability of known phases, but also reveal the stability of a family of previously unknown ordered phases that combine features of $L1_2$ and $L1_0$ in different ratios to adjust their overall composition. The calculations also confirm the stability of vacancy ordered B2 derivatives that are stable in the Al rich half of the phase diagram. We introduce strain order parameters to systematically analyze instabilities with respect to the Bain path connecting the FCC and BCC lattices. Many unstable orderings on both FCC and BCC are predicted around compositions of $x_{Ni} = 0.625$, where a martensitic phase transformation is known to occur. Cluster expansion techniques together with Monte Carlo simulations were used to calculate a finite temperature-composition phase diagram of the Ni-Al binary. The calculated phase diagram together with an analysis of Bain instabilities reveals the importance of anharmonicity in determining the phase bounds between the B2 based β phase and the $L1_2$ based γ' phase, as well as properties related to martensitic transformations that are observed upon quenching Ni rich β.

I. INTRODUCTION

Nickel based superalloys have found a wide range of industrial applications thanks to their high temperature mechanical properties and corrosion resistance [1]. The Ni-superalloys of turbine engines for propulsion and power generation usually contain many alloying additions, but primarily build on the Ni-Al binary. This binary has been studied extensively and contains a variety of intermetallic compounds with unique properties. The Ni rich phases of the Ni-Al binary are all orderings on an FCC parent crystal structure and include the Ni rich solid solution, γ, the γ'-Ni_3Al phase having $L1_2$ ordering and the Ni_5Al_3 phase. FCC ordering gives way to BCC orderings at equiatomic mixtures of Ni and Al where the β phase having B2 ordering on a BCC parent crystal structure is favored. Coherent two-phase mixtures consisting of γ and γ' are used to realize high strength and creep resistance at elevated temperatures[2], while the β phase, having favorable oxidation behavior, is used as a bond coat on turbine engine blades made of a superalloy core[3,4].

In contrast to most intermetallic compounds, the β phase can tolerate a high degree of off-stoichiometry through the introduction of antisite defects and vacancies[5]. β-NiAl accommodates excess Ni by forming antisite Ni defects on its Al sublattice. Ni rich β phases are susceptible to a martensitic transformation upon quenching[6], whereby the high temperature, Ni-rich B2 ordering on BCC transforms to an FCC variant through a diffusionless process[7–9]. Many fundamental questions remain about the thermodynamics and kinetics of these martensitic transformations. Excess Al in β-NiAl, in contrast, is realized with Ni vacancies on the Ni sublattice of the B2 ordering and can reach unusually high vacancy concentrations for an intermetallic compound. In fact the high vacancy concentrations can lead to vacancy ordering within the B2 crystal structure, however, the phase relations among the various vacancy ordered derivatives have yet to be established.

Here we report on a combined first-principles density functional theory (DFT) and statistical mechanics study of phase stability in the Ni-Al binary. We focus in particular in elucidating the thermodynamic properties of the Ni-Al binary at concentrations where the alloy transitions from FCC to BCC. To this end, we introduce strain order parameters to determine the onset of instabilities between FCC and BCC based orderings along the Bain path. These instabilities are discussed in the context of the observed martensitic transformation, which has been the subject of both experimental[7,8,10] and computational[11] work. We also investigate the thermodynamic properties associated with vacancy ordering over the Ni-sublattice of Al-rich β-NiAl and discover the stability of a family of hybrid phases that combine features of $L1_0$ and $L1_2$ in the Ni rich half of the Ni-Al binary.

II. METHODS

A. DFT calculations

First-principles density functional theory (DFT) calculations were performed to predict ordering preferences in the Ni-Al binary and to investigate instabilities with respect to the Bain path. All first-principles calculations were performed within the generalized gradient approximation (GGA-PBE) using the projector augmented wave (PAW) pseudopotential method[12] as implemented in the Vienna ab initio Simulation Package (VASP)[13–15]. The CASM[5,16–19] software package was used to enumerate symmetrically distinct orderings over FCC and BCC, allowing Ni and Al to occupy the FCC lattice, and Ni, Al and vacancies to occupy the sublattices of a BCC based

B2 ordering. A k-point mesh of $23 \times 23 \times 23$ was found to converge the energy of a FCC primitive Ni cell to within 1meV per atom, while a density of $17 \times 17 \times 17$ was found to do the same for a NiAl B2 cell. The k-point meshes for the configurations enumerated in supercells of FCC Ni and of B2 NiAl were scaled appropriately to maintain the same k-point density. All DFT-PBE calculations were initialized with a spin polarized ferromagnetic ordering[20]. To ensure accuracy in our calculations, a plane wave energy cutoff of 560eV was used. Numerical k-space integration through the Brillouin zone was performed using a smearing parameter of 0.2eV with the Methfessel-Paxton method (first order). The DFT-PBE energies were calculated allowing atomic positions and lattice parameters to relax to minimize the total energy.

B. Metrics of relaxation and Bain instabilities

With the exception of Al_3Ni, every phase in the Ni-Al binary can be described as an ordering over either an FCC or BCC lattice. Most orderings over FCC or BCC break the original cubic symmetry of their parent crystal. These configurations therefore relax into structures that lack the initial connectivity between atoms of their ideal parent crystal structure. Every atom in FCC, for example, has exactly 12 nearest neighbors, while each atom in BCC has 8 nearest neighbors. Upon relaxation, the atomic connectivity of configurations with broken symmetry usually differ only slightly from that in the undistorted starting crystal, largely retaining the same number of nearest neighbors within a small tolerance. These configurations are dynamically stable and represent the lowest energy state for that ordering on the starting parent crystal structure. However, particular decorations on FCC and BCC may be dynamically unstable, undergoing significant deformation when relaxing atomic coordinates and lattice vectors during energy minimization. They change their connectivity to the point that the resulting structure more closely resembles a different parent crystal structure from the one they started on.

Strain can serve as an order parameter to track the extent of lattice relaxation. A reference lattice with vectors $\vec{a}$, $\vec{b}$ and $\vec{c}$

$$\mathbf{L} = \begin{bmatrix} a_x & b_x & c_x \\ a_y & b_y & c_y \\ a_z & b_z & c_z \end{bmatrix} \tag{1}$$

is related to a deformed lattice $\mathbf{L}'$ by a deformation gradient tensor $\mathbf{F}$ according to

$$\mathbf{L}' = \mathbf{F}\mathbf{L}. \tag{2}$$

This deformation tensor can be factored into a rotation $\mathbf{R}$ and a symmetric stretch tensor $\mathbf{U}$ using polar decomposition as

$$\mathbf{F} = \mathbf{R}\mathbf{U}. \tag{3}$$

Because $\mathbf{R}$ corresponds to a rigid body rotation, the energy of the crystal is unaffected by it, and any metric of strain should depend only on the stretch tensor $\mathbf{U}$. The rotation $\mathbf{R}$ can be eliminated by multiplying $\mathbf{F}$ by its transpose (since $\mathbf{R}^{-1} = \mathbf{R}^{\intercal}$), yielding the commonly used right Cauchy-Green stretch tensor[21]

$$\mathbf{U}^2 = \mathbf{F}^{\intercal}\mathbf{F} \tag{4}$$

There are several strain tensors that can be defined in terms of the stretch tensor $\mathbf{U}$. In this study, we use the Hencky strain defined as

$$\mathbf{E} = \ln \mathbf{U}. \tag{5}$$

Similar to $\mathbf{U}$, this strain metric is also symmetric, with only 6 independent strain components

$$\mathbf{E} = \begin{bmatrix} \varepsilon_{xx} & \varepsilon_{xy} & \varepsilon_{xz} \\ \varepsilon_{xy} & \varepsilon_{yy} & \varepsilon_{yz} \\ \varepsilon_{xz} & \varepsilon_{yz} & \varepsilon_{zz} \end{bmatrix} = \mathbf{E}^{\intercal} \tag{6}$$

However, instead of working directly with the six independent Hencky strain elements of eq. (6), it is more convenient to use an equivalent set of symmetry adapted strain metrics defined as linear combinations of the Hencky strains according to[22]:

$$e_1 = \frac{\varepsilon_{xx} + \varepsilon_{yy} + \varepsilon_{zz}}{\sqrt{3}} \tag{7}$$

$$e_2 = \frac{\varepsilon_{xx} - \varepsilon_{yy}}{\sqrt{2}} \tag{8}$$

$$e_3 = \frac{2\varepsilon_{zz} - \varepsilon_{yy} - \varepsilon_{xx}}{\sqrt{6}} \tag{9}$$

$$e_4 = \sqrt{2}\varepsilon_{yz} \tag{10}$$

$$e_5 = \sqrt{2}\varepsilon_{xz} \tag{11}$$

$$e_6 = \sqrt{2}\varepsilon_{xy} \tag{12}$$

e_1 is a measure of dilation, and is proportional to the volume change provided the Hencky strain metric is used. It is for this reason that we use the Hencky strains, as it uncouples any volume dependence from e_2-e_6. The e_2 and e_3 strains together describe tetragonal and orthorhombic distortions of the crystal, while the e_4,e_5 and e_6 strains represent shears.

A common instability for both FCC and BCC based orderings is the Bain path. The above symmetry adapted strain metrics enable a representation of all symmetrically equivalent Bain paths that connect FCC to BCC in the two dimensional space spanned by e_2 and e_3. A conventional FCC cell with its cubic axes oriented along the

x-y-z Cartesian directions can be transformed to BCC by a contraction along the z direction and a simultaneous expansion along the x and y directions. The Bain path along the z axis is most easily visualized with a 2 atom tetragonal FCC unit cell as shown in fig. 1. There are three symmetrically equivalent Bain paths as a result of the cubic symmetry of an FCC crystal. Equivalent transformations can be realized by contracting along the y direction and expanding along the z and x directions, or by contracting along the x direction and expanding along the y and z directions. The Bain path involving a compression along the z-direction (fig. 1) follows the negative e_3 axis, holding e_2=0 when using FCC as a reference for strain. The two other symmetrically equivalent Bain paths follow the dashed lines of fig. 2, which are related to the e_3 axis by 120° rotations in e_2-e_3 space. The dashed lines in e_2-e_3 space in fig. 2 correspond to tetragonal distortions of the reference FCC lattice, while any other points that deviate from these lines correspond to orthorhombic distortions of FCC. When using Hencky strains, any distortion corresponding to a path in this space at fixed e_1 occurs at constant volume.

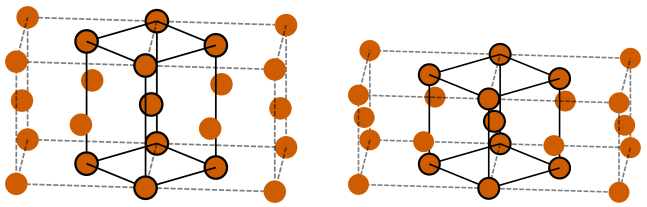

(a) (b)

FIG. 1. A Bain transformation from a FCC (fig. 1a) to a BCC (fig. 1b) crystal structure. The transformation of this FCC ordering corresponds to a path in the negative e_3 direction.

Strain transformations from BCC to FCC can also be mapped out in e_2-e_3 space using the BCC crystal as the reference to measure strain. The axes of the conventional cubic BCC unit cell must be aligned along the x-y-z directions. The BCC crystal then resides at the origin in e_2-e_3 space. The pathways are the same as the Bain paths described for FCC, but are taken in the opposite direction: a path in the positive e_3 direction with no e_2 contribution results in an expansion in the z direction and a contraction in the x and y directions. There are three equivalent paths in e_2-e_3 space that convert BCC into FCC. These paths are also related to each other by 120° rotations in e_2-e_3 space as illustrated in Figure 3(b).

While the Bain path can be fully described in terms of strains, many other paths connecting a pair of parent crystal structures combine a lattice strain with an internal shuffle of the basis atoms within the unit cell. An example is the Burgers path[23], which connects BCC to HCP. To map relaxed orderings onto their closest parent crystal structure, we therefore rely on a composite score that is a function of both the strain (deformation) of the unit cell vectors as well as the displacements of the basis atoms within the unit cell. A deformation score is

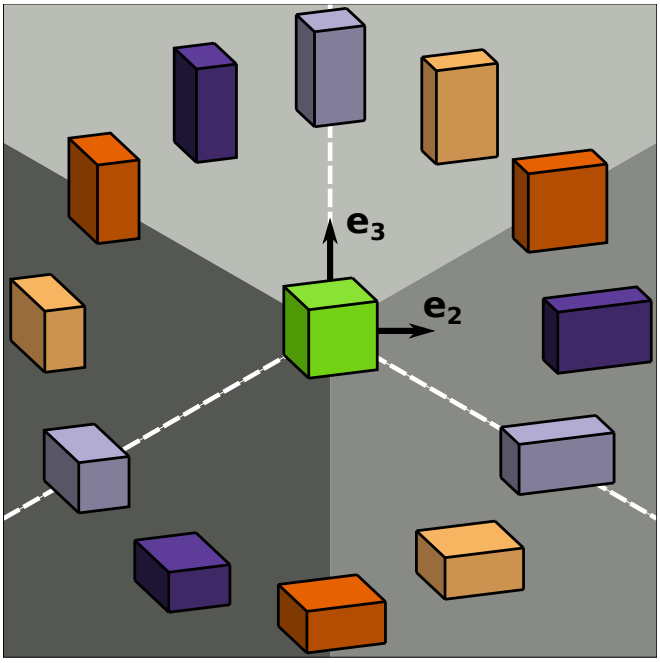

FIG. 2. Schematic of the possible deformations in e_2-e_3 space relative to a cube. All deformations preserve the volume of the reference structure, with distortions along dashed lines being purely tetragonal. Shapes that share the same color have had a symmetrically equivalent deformation applied along different directions, resulting in identical structures that differ only by a spatial rotation.

defined as proportional to the sum of the squares of the Biot strain after removal of any volumetric expansion or contraction, i.e. $\mathbf{U}/\det(\mathbf{U}) - \mathbf{I}$ where $\mathbf{U}$ is the symmetric stretch tensor and $\det(\mathbf{U})$ relates the relaxed volume to the reference volume. A displacement score is defined as the sum of the squares of the displacements (normalized by the number of atoms in the unit cell) relative to the ideal positions of the prototype crystal having relaxed unit cell vectors. A weighted sum of the deformation and displacement score is then used to assign a relaxed configuration to the prototype it most closely maps onto. An in depth description can be found in the work of Thomas et al[24].

In this study, we compared all relaxed configurations to ideal FCC, BCC and HCP parent crystal structures. In the strictest sense, the great majority of orderings will not be perfect FCC, BCC or HCP, as they will lack cubic and hexagonal symmetry. Nevertheless, we will refer to relaxed orderings as FCC, BCC or HCP depending on which of these parent crystal structures they are most closely related to.

C. Cluster Expansion Method

Phase stability at finite temperature was studied using cluster expansions to extrapolate first-principles DFT

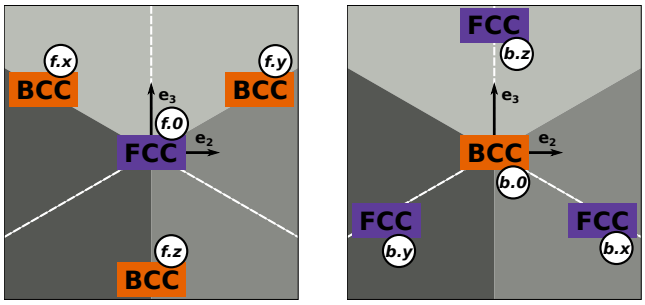

(a) (b)

FIG. 3. Bain paths relative to FCC (fig. 3a) and BCC (fig. 3b) structures in e_2-e_3 space holding all other strain metrics constant. The origin represents the unstrained crystal and can take three symmetrically equivalent Bain paths to transform from FCC/BCC to BCC/FCC. The locations in e_2-e_3 space that correspond to FCC and BCC structures are labelled for reference throughout this work. The origin (reference structure) is indicated by a "*0*", while strain values at the end of equivalent Bain paths are indicated by "x", "y" or "z". Labels beginning with "f" correspond to strain values relative to a FCC structure, while labels beginning with "b" correspond to strains relative to BCC.

energies within Monte Carlo simulations. A cluster expansion describes the energy of a multicomponent crystal as a function of its degree of order/disorder. For binary solids, occupation variable σ_i are assigned to each crystal site i that take on a value of 0 or 1 depending on the occupant of the site (e.g. Ni vs Al). A particular arrangement over the N-sites of a crystal is then specified by the collection of occupation variables $\vec{\sigma} = \{\sigma_1, \sigma_2, \cdots, \sigma_N\}$. The dependence of the energy of the crystal on arrangement, $\vec{\sigma}$, can be written as [25–27]

$$E_f(\vec{\sigma}) = \sum_\alpha V_\alpha \phi_\alpha(\vec{\sigma}) \tag{13}$$

where ϕ_α are cluster basis functions defined as

$$\phi_\alpha(\vec{\sigma}) = \prod_{i \in \alpha} \sigma_i \tag{14}$$

and correspond to products of occupation variables belonging to sites of clusters α, which include point, pair, triplet etc. clusters. The coefficients V_α are expansion coefficients called effective cluster interactions (ECI) and need to be determined from first principles.

While the sum in Eq. 13 extends over all clusters of sites α within the crystal, to be practical, it must be truncated at a particular cluster size and radius. The ECI of Eq. 13 can then be fit to the DFT energies of a set of symmetrically distinct configurations using one of several inversion methods[28,29]. First-principles parameterized cluster expansions usually require only a relatively small number of nonzero ECI to accurately predict the formation energy of any configuration. With an accurate cluster expansion it is possible to rapidly evaluate the formation energy within Monte Carlo simulations to calculate thermodynamic averages. In this study of the Ni-Al binary, two cluster expansions were constructed, one for the FCC parent crystal and one for sublattice disorder in B2, which it self is an ordering over the BCC parent crystal structure. The construction and parameterization of the cluster expansion and the Monte Carlo simulations were performed with the CASM software package[5,16–19].

III. RESULTS

A. Formation Energies

The first step to understanding the thermodynamics of the Ni-Al system from first principles is to establish the ground states at zero Kelvin. A large number of orderings on the FCC and BCC lattice were systematically enumerated within symmetrically distinct supercells. FCC configurations were enumerated from a one atom FCC primitive cell, allowing either Ni or Al to occupy each site. BCC configurations were enumerated relative to a B2 (2 atom) primitive cell. Previous studies[5,30–33] showed that off stoichiometry in B2 NiAl is accommodated by vacancies on the Ni sublattice and by Ni antisite defects on the Al sublattice. For this reason, the occupancy of the enumerated BCC configurations were limited to allow Ni-Va disorder on one sublattice and Al-Ni disorder on the other.

Figure 4 shows the calculated formation energies of all enumerated configurations over FCC and B2. Formation energies were calculated relative to pure FCC Ni and FCC Al, and were normalized per number of atoms according to

$$E_f = \frac{E^{DFT} - N_{Al}E^{DFT}_{Al} - N_{Ni}E^{DFT}_{Ni}}{N_{Al} + N_{Ni}} \tag{15}$$

Throughout we will use atomic fraction, defined as

$$x_{Ni} = \frac{N_{Ni}}{N_{Ni} + N_{Al}} \tag{16}$$

as our composition variable. The vertices of the convex hull (dashed line in fig. 4) of the formation energies correspond to the lowest energy groundstates, which are line compounds at 0 K.

Pure Ni ($x_{Ni} = 1$) is stable in the FCC crystal structure. At finite temperature it can dissolve Al, forming the Ni rich solid solution that is referred to as the γ phase. The next vertex of the convex hull at $x_{Ni} = 0.75$ in Figure 4 is the $L1_2$ ordering, commonly referred to as γ'. The unit cell for this ordered phase can be constructed by replacing the corners of a Ni FCC conventional cell with Al, which preserves cubic symmetry (fig. 5b). The ground state at x_{Ni}=0.625 has orthorhombic symmetry and corresponds to the experimentally characterized phase Ni_5Al_3[5,8], referred to in this work as δ. In addition to δ and γ', there is a large number of configurations between x_{Ni}=0.625 and 0.75 that also have low formation

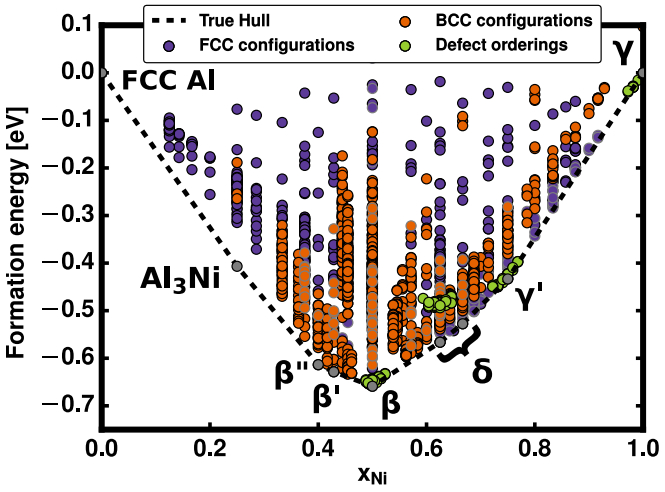

FIG. 4. Calculated formation energies relative to FCC Ni and FCC Al. Configurations stable as a BCC structure are shown in orange, while configurations stable as a FCC structure are shown in purple. Groundstates have been colored gray and are connected by the convex hull of the energies.

energies. One of these configurations, having a composition of $x_{Ni} = \frac{2}{3}$, is a groundstate, residing on the convex hull. Many others have energies that are only several meV above the convex hull. We elaborate on the orderings of these structures and their relation to the δ phase in section III B.

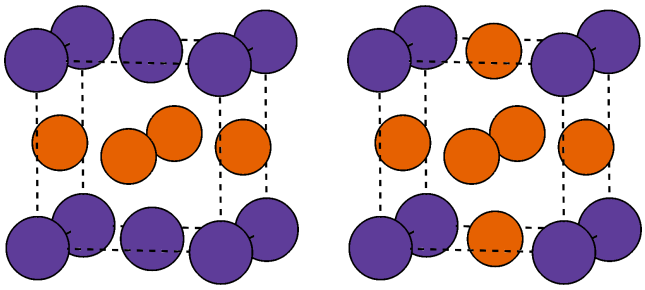

FIG. 5. Unit cells for the unstable $L1_0$ ordering (fig. 5a) and the $L1_2$ ordering of the γ' phase (fig. 5b). The ordering of $L1_0$ on the FCC crystal reduces the symmetry from cubic to tetragonal, while $L1_2$ preserves cubic symmetry. Ni atoms are shown in orange, while Al atoms are shown in purple.

The next set of ground states are all BCC based orderings. At $x_{Ni} = 0.5$, perfect B2 ordering is stable in which the corners of a conventional BCC unit cell are occupied by Ni and the body center is occupied by Al. Remarkably, two additional B2 derived ground states exist that are Al rich. Both can be viewed as B2 superstructures with vacancy ordering over the Ni sublattice. The first, having chemical formula Ni_3Al_4, has cubic symmetry, a full Al sublattice, and vacancy pairs ordered in a three dimensional pattern. This ordering requires a $4 \times 4 \times 4$ B2 supercell and was not enumerated directly, but was taken from the work of Ellner et al[34]. It is isostructural with the Ni_3Ga_4 compound. The vacancies are arranged in such a manner that any row of the Ni sublattice in B2 along any of the x, y or z directions has three filled sites followed by a single empty one, as shown in fig. 6c. The second B2 derived ground state, having chemical formula Ni_2Al_3, is even more Al rich as a result of a higher vacancy concentration on the Ni sublattice. The vacancy ordering in Ni_2Al_3 is achieved by removing every third Ni layer of B2 along the {111} direction. In the literature, stoichiometric B2-NiAl is referred to as the β phase. In view of their similarity to B2, we will refer to Ni_3Al_4 and Ni_2Al_3 as β' and β'' respectively in the remainder of the text.

The final intermetallic ground state, Al_3Ni, is distinctly different from all the other phases of the Ni-Al binary as it cannot be mapped to a particular ordering on FCC or BCC. Instead, it has the $D0_{20}$ structure, which is isomorphic with Fe_3C (cementite) and has orthorhombic symmetry.

As with pure Ni, pure Al is also stable in FCC. In contrast to pure Ni and the intermetallic compounds in the Ni-Al binary, though, FCC Al has a low melting temperature of around 660°C.[35]

In addition to enumerating different orderings in small supercells (containing up to 8 atoms for FCC and 16 atoms for BCC), we also systematically enumerated anti-site defects in large supercells of the ground state orderings. Supercells of $L1_2$, B2 and δ were perturbed with point, pair and triplet antisite defects. To minimize interactions between periodic images of the anti-site defects, supercells containing 108 atoms for $L1_2$, 96 atoms for δ, and 128 atoms for B2 were used. The formation energies for these orderings are depicted in green in fig. 4 and fig. 7. While the formation energies of supercells containing anti-site defects are normalized by the number of atoms in the supercell and their distance from the convex hull is not a direct measure of anti-site defect formation energies, fig. 4 and fig. 7 clearly show a large qualitative difference in anti-site defect formation energies between $L1_2$ and B2 on the one hand, and δ on the other. The formation energies for dilute antisite defects in $L1_2$ and B2 supercells all have values that are only slightly above the convex hull. The opposite is true for anti-site defects in δ, which have formation energies that are substantially above the convex hull. This suggests that while $L1_2$ and B2 may tolerate anti-site disorder at elevated temperature, δ will not and will behave as a line compound.

B. An infinity of groundstates

The calculated formation energies of Figure 4 and Figure 7 show that there are a large number of configurations between $0.625 < x_{Ni} < 0.75$ having formation energies that lie below the common tangent between δ at x_{Ni}=0.625 and γ' at x_{Ni}=0.75. The final relaxed crystal

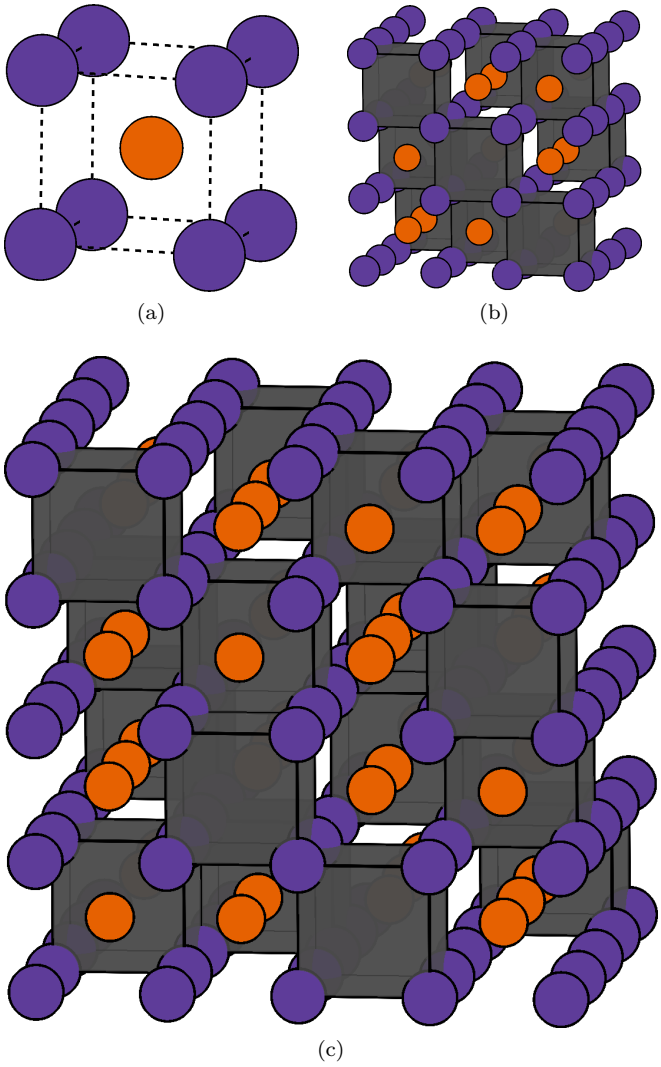

FIG. 6. Unit cells for the β (fig. 6a), β' (fig. 6c) and β'' (fig. 6b) phases. All three phases have an underlying B2 ordering, with Ni (orange) and Al (purple) atoms arranged on a BCC crystal. The β' and β'' phases have ordered vacancies on the Ni sublattice, shown with black boxes.

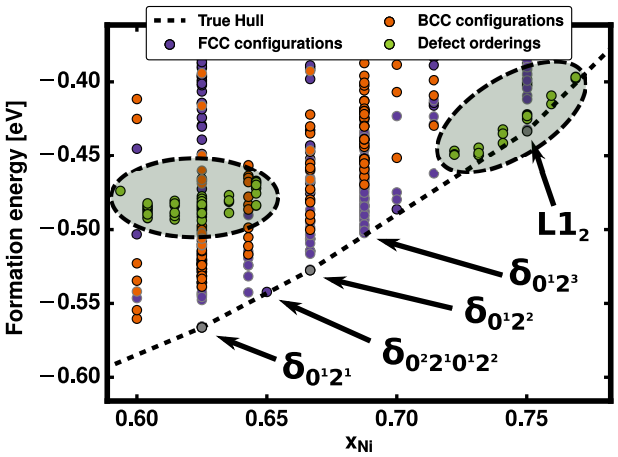

FIG. 7. Close up of formation energies near δ and γ' compositions. Configurations that are combinations of $L1_0$ and $L1_2$ result in new groundstates that break the convex hull. Energies colored green correspond to orderings of $\delta_{0^1 2^1}$ and $L1_2$ with a dilute amount of antisite defects. Dilute defect energies in the $\delta_{0^1 2^1}$ and $L1_2$ orderings have been highlited.

structures for each of these configurations were found to most closely map onto FCC. Examination of their atomic positions and arrangements revealed that they can be viewed as hybrids of $L1_0$ and $L1_2$ orderings. The crystal structures of $L1_0$ and $L1_2$ are compared in fig. 5. $L1_0$ consists of alternating Ni and Al layers along the {001} direction of FCC. $L1_2$ can be derived from $L1_0$ by replacing half the Al in the Al (001) layers of $L1_0$ by Ni in a checker board pattern.

The δ ordering at $x_{Ni} = 0.625$, which is the first ground state of the series of hybrid orderings (Figure 7), is made up of alternating layers of $L1_2$ and $L1_0$ along the {101} direction as illustrated in fig. 8. Additional layered configurations were systematically enumerated by varying the number and order of $L1_0$ and $L1_2$ layers along the {101} direction. Configurations with single $L1_0$ layers separated by one or more $L1_2$ layers were found to have formation energies that dip below the common tangent connecting δ at $x_{Ni} = 0.625$ and $L1_2$ at $x_{Ni} = 0.75$. Aluminum rich configurations having an excess of $L1_0$ layers in contrast were found to have high formation energies that are substantially above the common tangent between δ at $x_{Ni} = 0.625$ and B2 NiAl at x_{Ni}=0.5.

Hybrid orderings are common in alloys and oxides[19,36–38]. A naming convention has been established to label families of hybrid phases[36], which we adopt here. Since the first hybrid phase Ni_5Al_3 is referred to as δ, we use this label to refer to the whole family of hybrid orderings. Subscripts are then added to distinguish the various hybrid orderings based on their number of $L1_2$ and $L1_0$ subunits. A "0" indicates a $L1_0$ layer, while a "2" indicates a $L1_2$ ordering. Exponents on each subscript denote the number of each layer used to construct the full ordering. The unit cell of the groundstate at $x_{Ni} = \frac{2}{3}$, for example, is composed of a single $L1_0$ layer followed by two $L1_2$ layers (fig. 8). This groundstate is, therefore, labeled as $\delta_{0^1 2^2}$. The ground state at $x_{Ni} = 0.625$, Ni_5Al_3, consists of alternating layers of $L1_0$ and $L1_2$, such that its label would be $\delta_{0^1 2^1}$.

C. Navigating strain space

Many orderings on FCC and BCC in the Ni-Al binary are dynamically unstable and relax to a different parent crystal structure.[39] The strain order parameters described in section II B can be used to quantify the distance of a relaxed structure to either FCC or BCC. We

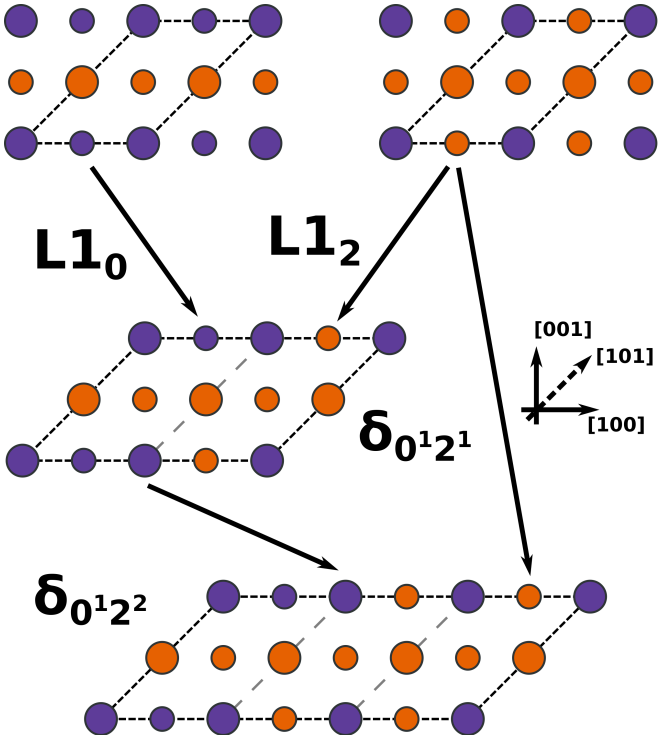

FIG. 8. $L1_0$ (left) and $L1_2$ (right) orderings and their relation to the Ni_5Al_3 δ structure (bottom). Alternating layers of $L1_0$ and $L1_2$ unit cells along the [101] plane result in the $\delta_{0^1 2^1}$ and $\delta_{0^1 2^1}$ ordering.

systematically analyze relaxation strains in this section. High symmetry points and lines in e_2-e_3 space will be referred to using the labelling outlined in fig. 3.

1. *Pure Ni (γ) and $L1_2$ (γ') strain surface*

The simplest phase to explore in e_2-e_3 space is pure Ni (γ phase) as it lacks a symmetry breaking Ni-Al ordering. Wang et al[39] have already shown that if a pure element is stable as FCC at 0K, then the BCC form of that element must be unstable. The global energy minimum for Ni lies at the origin (fig. 9, located at *f.0*) when using FCC as a reference for strain. Three equivalent Bain paths connect FCC at the origin to three symmetrically equivalent BCC lattices (*b.z*, *b.y*, *b.x*). These equivalent BCC lattices appear as three saddle points (instabilities along the Bain path) on the energy surface. Extending further along these Bain paths yields a local minimum, corresponding to a BCT structure, consistent with the findings of Wang et al[39].

The γ' phase, having $L1_2$ ordering, has FCC connectivity, and is the groundstate when $x_{Ni} = 0.75$. The global minimum for the strain energy plot of the γ' phase (fig. 10) using FCC as a reference again resides at the origin (*f.0*). The $L1_2$ ordering preserves the original FCC cubic point group symmetry, reflected in the threefold

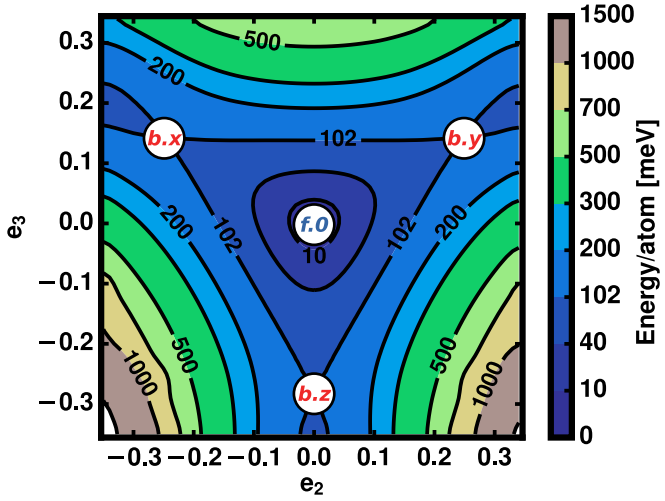

FIG. 9. Strain energies relative to FCC Ni. Strain values corresponding to FCC are indicated with *f*, while values corresponding to BCC are shown with *b*. Any straight path connecting the origin to a marked location is a Bain path.

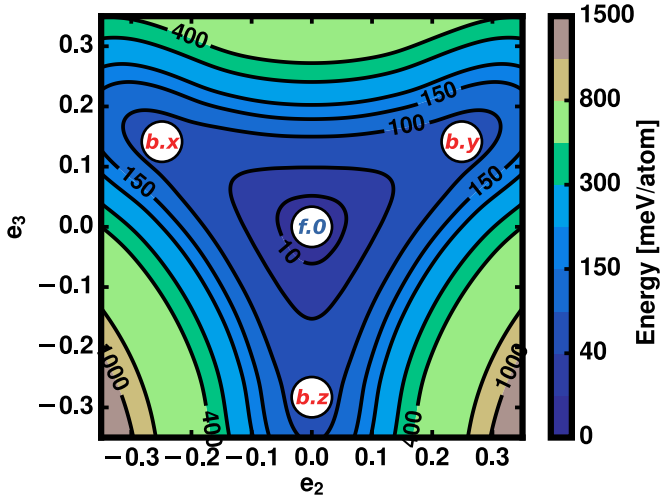

FIG. 10. Strain energies relative to the $L1_2$ ordering.

symmetry of the energy surface in e_2-e_3 space. The BCC variants (indicated by locations *b.z*, *b.y*, *b.x*) do not reside in a local minimum and are therefore unstable and will spontaneously relax back to FCC $L1_2$.

2. *B2 (β) strain surface*

The β phase has a B2 ordering on the BCC crystal structure. Figure 11a shows that its energy is at a global minimum at the origin in e_2-e_3 space (*b.0*) when B2 is used as the reference for strain. This structure also has cubic symmetry, which is once again reflected in the 3-fold symmetry in e_2-e_3 space. Straining B2 along any

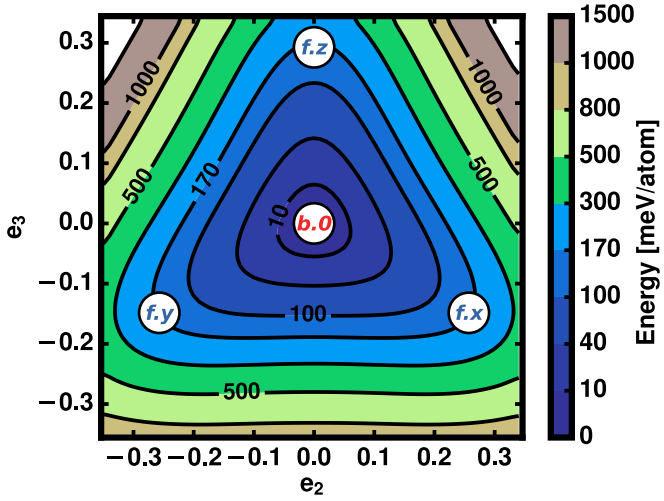

(a)

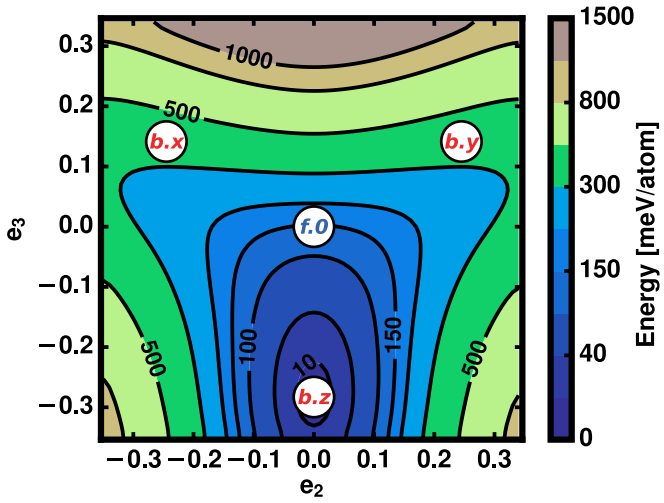

(b)

FIG. 11. Strain energies relative to the B2 ordering (fig. 11a) and the $L1_0$ ordering (fig. 11a). Non B2 based BCC orderings are mechanically unstable.

of the three Bain paths results in three equivalent FCC $L1_0$ orderings (*f.z*, *f.y*, *f.x*). The plot reveals that these three FCC variants do not coincide with any local minima and will spontaneously collapse to the BCC B2 ordering. NiAl having $L1_0$ ordering is therefore mechanically unstable.

Interesting properties are revealed about Ni-Al orderings on BCC when using FCC $L1_0$ as a reference for strain. Since the Ni-Al ordering in $L1_0$ (fig. 5a) has tetragonal symmetry, the three-fold symmetry in e_2-e_3 space is broken (fig. 11b). One Bain path connects $L1_0$ (*f.0*) to the B2 ordering on BCC (*b.z*), and the two other Bain paths connect symmetrically equivalent orderings on BCC (*b.x*, *b.y*) consisting of alternating Ni and Al layers along the {110} directions, as shown in fig. 12. As is clear in fig. 11b, not only is $L1_0$ at the origin unstable (*f.0*), the two non-B2 Ni-Al orderings (fig. 12, residing on *b.x* and *b.y*) are also unstable. Figure 11b shows that alternating layers of Ni and Al along {110} in BCC will spontaneously collapse to a B2 ordering, which is also BCC. This is an example where an instability of an ordering on BCC causes a structural relaxation to another ordering on BCC (fig. 12).

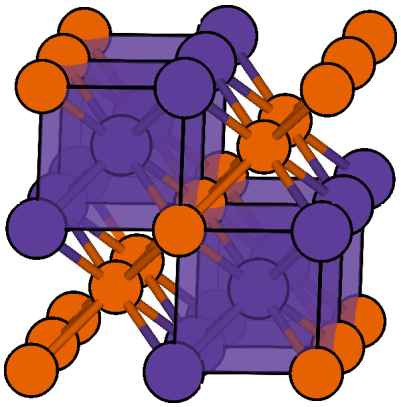

FIG. 12. Unstable ordering on BCC. Alternating Ni and Al layers along {110} directions will spontaneously relax into the favorable B2 ordering. The ordering shown here corresponds to strain locations *f.y* and *f.x* in fig. 11b.

3. $\delta_{0^1 2^1}$ strain surface

Strain energy surfaces in e_2-e_3 space for δ Ni_5Al_3 (i.e. $\delta_{0^1 2^1}$) are shown in fig. 13. Figure 13a shows the strain energy surface when using FCC as a reference for strain. As is clear in fig. 13a, the minimum of the energy surface does not reside at the origin corresponding to perfect FCC (*f.0*), but is shifted due to the orthorhombic symmetry of the Ni-Al ordering of $\delta_{0^1 2^1}$. The three Bain distortions that originate from FCC are therefore also no longer symmetrically equivalent. While the three BCC orderings that can be generated by application of Bain distortions to $\delta_{0^1 2^1}$ are all dynamically unstable (fig. 13a), one of the BCC variants (*b.z*) clearly resides in a more shallow energy valley than the two others. Interestingly, the energies of the $\delta_{0^1 2^1}$-ordering of ideal FCC and of ideal BCC in the lowest energy valley are very close to each other, and have a low value of roughly 30meV/atom above the global minimum.

It is also revealing to consider the strain energy surface using the BCC variant in the lowest energy valley (*b.z* of fig. 13a) as a reference, shown as *b.0* in fig. 13b. While the minimum of the strain energy surface of fig. 13b resides close to the FCC variant corresponding to $\delta_{0^1 2^1}$ (*f.z*), the energy surface is nevertheless very shallow even for the other FCC variants (*f.x*, *f.y*) that can be reached by application of Bain distortions to the BCC variant at the origin of fig. 13b. Furthermore, it illustrates that there are two orderings on FCC at $x_{Ni} = 0.625$ (i.e. *f.x* and *f.y* in fig. 13b) that are dynamically unstable and

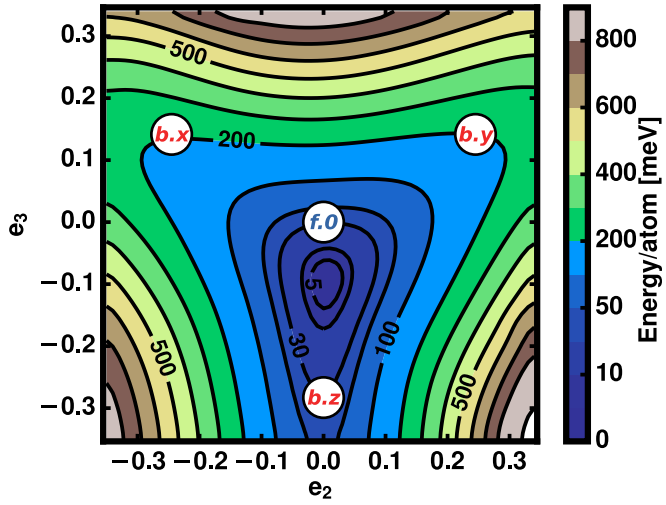

(a)

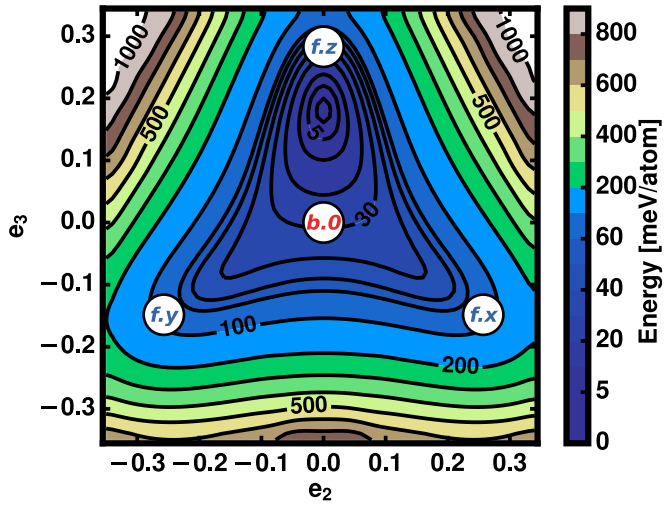

(b)

FIG. 13. Strain energy values for the $\delta_{0^1 2^1}$ ordering on FCC (fig. 13b) and BCC (fig. 13b). Unlike other groundstates, the global minimum for this structure is neither FCC (*f.0*) or BCC (*b.0*).

that, instead of collapsing to a BCC structure along a Bain path, will relax to another ordering on FCC (i.e. $\delta_{0^1 2^1}$, located at *f.z*). The shallow strain energy surface and its strong deviation from parabolic behavior, along with dynamical instabilities not only of BCC, but also of FCC orderings, indicates a strong degree of anharmonicity at compositions around $x_{Ni} = 0.625$. The strain energy surfaces of fig. 13a suggest that the alloy exhibits ambiguity about its preference for either FCC or BCC. Since the minimum of the energy surface lies closer to FCC than to BCC, the $\delta_{0^1 2^1}$ phase will resemble FCC more than BCC at low temperatures. At elevated temperature, though, anharmonicity may shift the lattice dimensions more towards BCC. We revisit this point when discussing phase stability at finite temperature.

D. Relaxation of enumerated structures

The previous section showed examples where a particular ordering on FCC will spontaneously relax along a Bain path to BCC and vice versa. Quantifying the amount of strain experienced by a particular ordering during relaxation does not require a full mapping of the energy surface in e_2-e_3 space as was done in the previous section. Only the minimum energy strains relative to the ideal reference parent crystal are needed, which are obtained by comparing the enumerated configuration before and after relaxation. For example, a Ni-Al arrangement on FCC having $L1_0$ ordering will relax into the BCC B2 ordering. The resulting relaxation strain coincides with the global minimum of fig. 11b. Figure 14 shows the relaxation strains of orderings enumerated over FCC and over the sublattices of BCC based B2 relative to their ideal starting parent structure. Each relaxation has been color coded to indicate the prototype structure (FCC, BCC or HCP) it most closely maps onto as determined using the metrics outlined in section II B.

Figure 14 shows that structures with small relaxation strains mapped onto their original parent crystal structure, while those with very large relaxation strains mapped onto another parent crystal structure. Interestingly, without accounting for shear strains, a sharp transition between FCC and BCC is evident in fig. 14. Figure 14a shows that almost every FCC ordering with a relaxation strain beyond a e_2-e_3 radius of about 1.5 has transformed into a structure that resembles BCC more than FCC (see section II B). Similar behavior is evident in fig. 14b, which shows that BCC orderings with relaxation strains in e_2-e_3 space beyond a radius of about 1.2 more closely map onto FCC than BCC. The clustering of points in this space also reveals that many of the relaxations followed a Bain path. Especially the large relaxation strains tend to fall along the Bain path, resulting in clearly visible arms extending from the origin.

Whether or not a configuration on a particular crystal structure is mechanically unstable is strongly correlated with its concentration. The fraction of enumerated orderings that are unstable in different composition intervals is shown in the histograms and energy plots of fig. 15. Figures 15a and 15c plot relaxation histograms and formation energies for orderings that were enumerated over FCC, while figs. 15b and 15d only show results for orderings enumerated over B2.

The orderings enumerated on the FCC lattice are consistently stable at both high and low Ni compositions. At compositions close to x_{Ni}=0.5, however, many configurations relax from FCC into a B2 derived ordering. The most pronounced example already discussed is the relaxation of $L1_0$ ordering on FCC to B2 along a Bain path (fig. 11b). This configuration is the point with the lowest energy at a composition of 0.5 Ni. As the histogram of fig. 15a clearly shows, configurations on FCC with compositions close to that of β are increasingly likely to have an ordering that is unstable with respect to a Bain strain

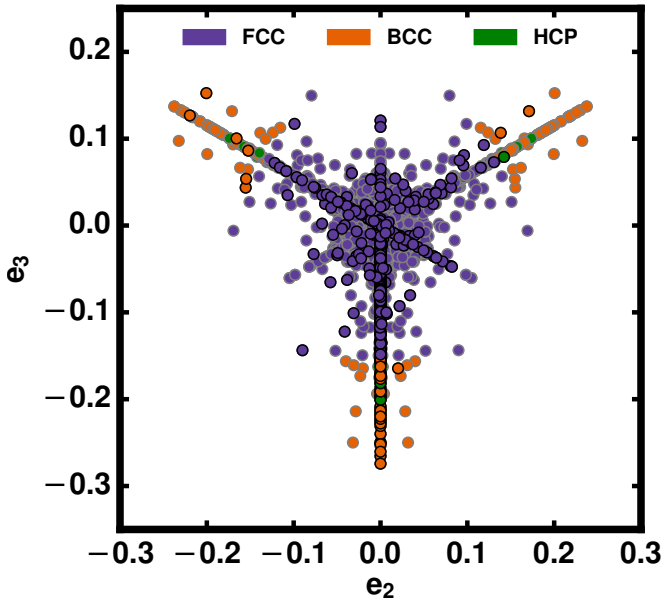

(a)

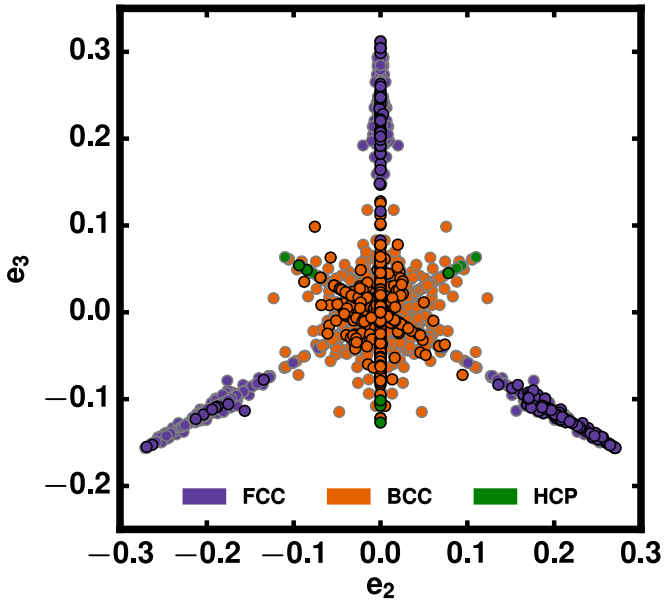

(b)

FIG. 14. For every enumerated configuration over FCC (fig. 14a) or B2 (fig. 14b) the strain of the relaxed structures is calculated relative to the structure used as input to DFT. This strain is then projected onto e_2-e_3 space. Orderings that undergo small e_2 and e_3 distortions appear closest to the origin. Combining the strain metrics with the Hungarian algorithm the relaxed structures are binned into FCC, BCC or HCP, indicated by the color of each point.

to BCC.

The configurations enumerated from the B2 unit cell also show an increase of instabilities within a narrow composition range. At compositions close to x_{Ni}=0.5, almost all of the lower energy structures maintain the original BCC parent lattice, but as the composition passes x_{Ni}=0.625 (i.e. the composition of the $\delta_{0^1 2^1}$), the majority of the enumerated B2 orderings (with mostly Ni antisites) collapse into FCC. The three groundstates in this composition range are either the FCC based γ and γ' phases, or the family of δ phases, which are more closely related to FCC than BCC. It is likely that many of the B2 orderings above $x_{Ni} = 0.625$ that maintain BCC connectivity after relaxation actually reside at a saddle point due to a high symmetry Ni-Al ordering. These phases would also be dynamically unstable, however, establishing this would require a phonon analysis for each structure which is beyond the scope of this study.

E. Cluster Expansion and finite temperature

The fully relaxed formation energies of different orderings on FCC and over the sublattices of B2 were used to parameterize cluster expansions. A cluster expansion allows us to rapidly extrapolate the DFT energies calculated for a small set of orderings to an arbitrary configuration in substantially larger supercells used in Monte Carlo simulations to calculate finite temperature thermodynamic averages. Two separate cluster expansions were constructed to describe the NiAl binary for $0.2 < x_{Ni} \leq 1$: one for B2 based orderings on BCC around $x_{Ni} = 0.5$, and another for Ni rich orderings on FCC. The sets of training data used to construct a cluster expansion should consist exclusively of orderings that are stable on their respective parent crystal structure. In fitting the cluster expansions, we therefore eliminated all configurations that relaxed to a different parent crystal structure.

The expansion for FCC contains 26 cluster basis functions and was fit to the energies of 539 orderings that mapped to FCC after relaxations. The expansion has a root mean square (rms) error of 0.015 meV/atom relative to the formation energies used in the fit and a cross validation (cv) score of 0.016 meV/atom. The FCC cluster expansion was weighted to more accurately predict formation energies of configurations having Ni rich compositions. The rms relative to DFT formation energies of configurations with $0.73 < x_{Ni} \leq 1$ is therefore lower having a value of 0.010 meV/atom.

The cluster expansion for B2 consists of 68 clusters and was fit to the energies of 892 enumerated orderings. The rms error for this fit is 0.012 meV/atom with a cv score of 0.028 meV/atom. All of the configurations for this cluster expansion were enumerated from a B2 unit cell, with different occupants allowed on the two sublattices: one sublattice accommodates Ni and vacancies, while the other accommodates Al and Ni. The use of a coupled cluster expansion[40,41] to describe disorder over two separate sublattices in β (B2-NiAl) was motivated by the early experimental observations of Bradley and Taylor[5] and more recent first-principles study[33,42]. These studies showed that B2-NiAl accommodates an excess of Ni with Ni anti-site defects on the Al sublattice and an

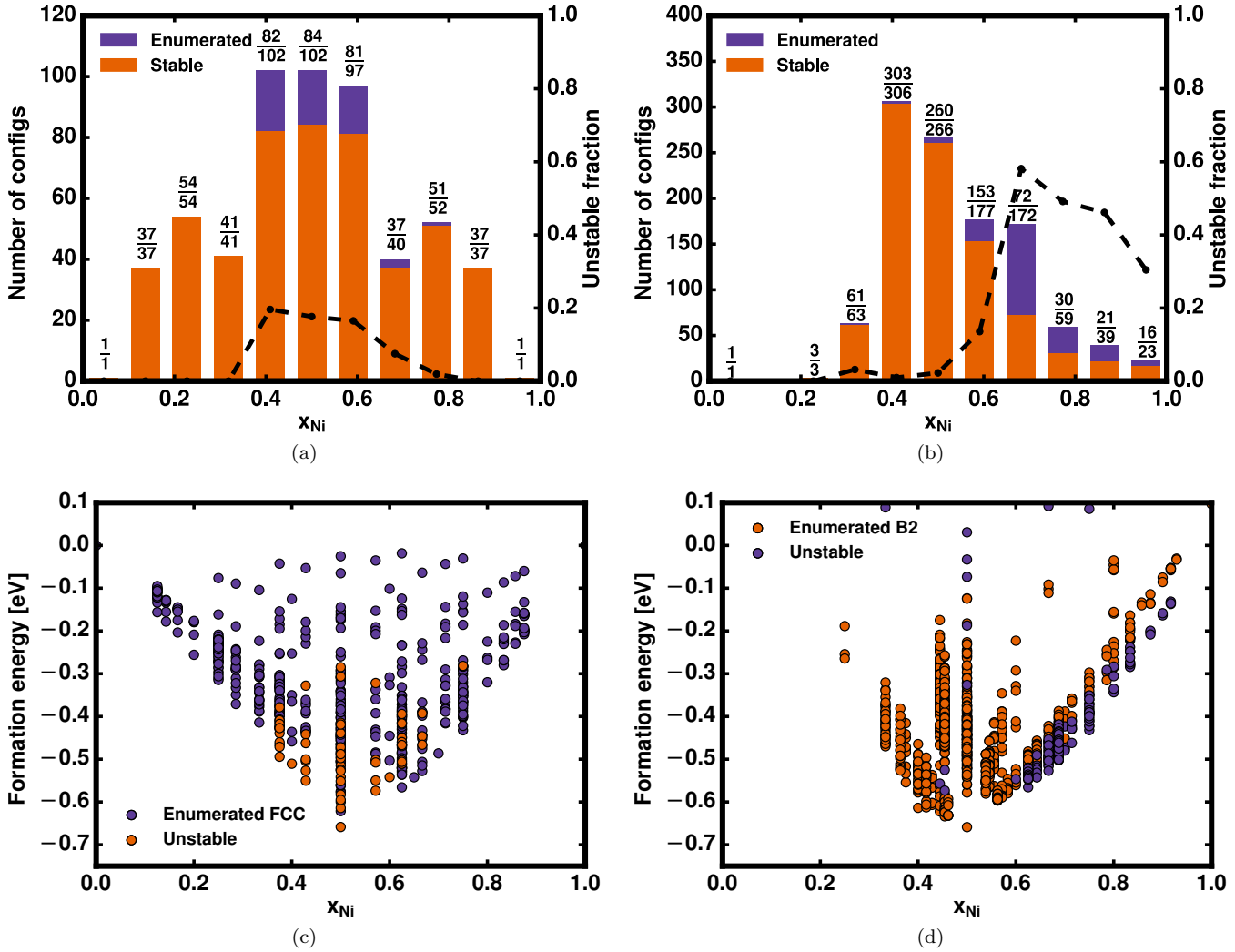

FIG. 15. Enumerated configurations over FCC (figs. 15a and 15c) and B2 (figs. 15b and 15d) comparing the amount of orderings that are stable.

excess of Al with vacancies on the Ni sublattice. While other anti-site defects also form, they are entropically stabilized and have exceedingly low compositions such that they do not affect bulk thermodynamic properties[33,42]. A cluster expansion that describes disorder relative to the B2 orderings on BCC as opposed to a general cluster expansion for the BCC lattice is also motivated by the strain energy surface of fig. 11b. As was pointed out in section III C, the B2 ordering of NiAl is especially stable with other simple orderings on BCC, such as the one depicted in fig. 12, being dynamically unstable and relaxing directly to B2.

The cluster expansions constructed to predict formation energies of orderings on FCC and B2 were subjected to grand canonical Monte Carlo simulations. In the grand canonical ensemble, the chemical potentials and temperature are controlled variables, while the conjugate variables, composition and grand canonical energy, are ensemble averages that can be approximated with Monte Carlo simulations. Free energies were obtained by integrating calculated relations between composition and chemical potential and between grand canonical energy and temperature[33,43]. Figure 16 shows calculated free energies as a function of composition at 705°C. Included in fig. 16 are the DFT formation energies of Al_3Ni, $\delta_{0^1 2^1}$ and $\delta_{0^1 2^2}$, which are treated as line compounds. As was shown in section III A, antisite defect formation is substantially more costly in $\delta_{0^1 2^1}$ than in B2-NiAl and γ'. The family of δ phases are therefore more resistant to antisite defects to realize off-stoichiometric compositions even at elevated temperatures and are approximated as line compounds.

Figure 17 shows a first-principles phase diagram for the Ni-Al binary obtained by minimizing calculated free energies through a common tangent construction at various temperatures. The liquid phase was not explicitly considered in the construction of the phase diagram, which should form in the yellow region of fig. 17 according to

experimental phase diagrams.[35] The orange regions in fig. 17 correspond to B2-derived single phase regions. The β phase, which has B2 ordering but no long-range vacancy ordering over the Ni-sublattice is stable around $x_{Ni} = 0.5$. The β' phase, having Ni_3Al_4 stoichiometry is stable at low temperature, but is predicted to decompose through a peritectoid reaction around 820°C. This phase, which as described in section III A is derived from B2 and exhibits long-range vacancy ordering on the Ni sublattice, is only stable in a narrow composition range. The β'' phase, which is also a vacancy ordered derivative of B2, is stable up to high temperatures and in a wide composition range. The purple single phase regions in fig. 17 correspond to FCC derived phases. The calculated phase diagram shows that the γ solid solution can tolerate a high Al concentration. The γ' phase, which has $L1_2$ ordering, is also stable in a wide concentration range with off-stoichiometry achieved with antisite defects. The two δ phases that reside on the convex hull, $\delta_{0^1 2^1}$ and $\delta_{0^1 2^2}$, appear as line compounds and, surprisingly, are predicted to remain stable up to high temperatures. The Al_3Ni phase was similarly treated as a line compound and also appears strictly at its stoichiometric composition in the phase diagram.

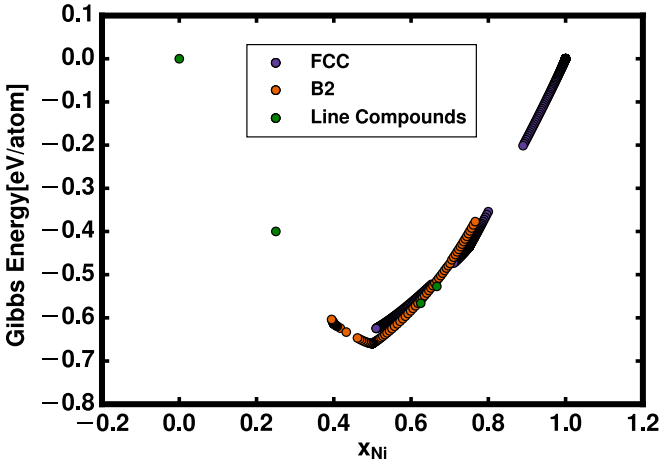

FIG. 16. Calculated Gibbs free energies for both the FCC (purple) and B2 (orange) cluster expansions at 705°C. Phases that are being approximated as a line compound (such as δ orderings) appear as a single green point.

IV. DISCUSSION

Our first-principles study of phase stability in the Ni-Al binary, both at zero Kelvin and at finite temperature, not only confirms the stability of the well characterized β and γ' intermetallic compounds, but also predicts a variety of ground states derived either from β for Al rich compositions, or from γ' for Ni rich compositions. The β phase, having B2-NiAl ordering, is unique among intermetallic compounds in that it can accommodate very

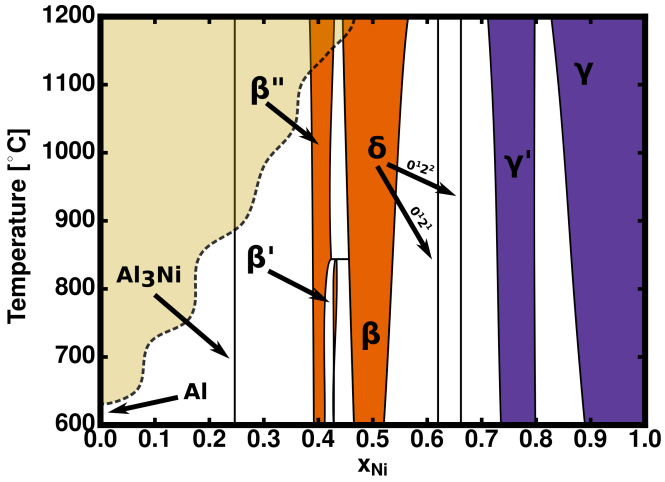

FIG. 17. Gibbs energy minimization for the binary system.

high concentrations of vacancies. While vacancy concentrations in intermetallic compounds typically do not exceed[44,45] 10^{-6} they can reach a fraction as high as 0.3 on the Ni sublattice of the β phase. Interactions among vacancies become important at such high concentrations, which in the β phase lead to two vacancy ordered derivative phases of β. At Ni rich compositions, a hierarchy of hybrid phases, consisting of layers of $L1_0$ and $L1_2$ ordering having different ratios are predicted as ground states or near ground states between $x_{Ni} = 0.625$ and 0.75. The energy of these phases as a function of strain order parameters that describe all symmetrically equivalent Bain paths are very shallow. These strain energy surfaces show that the hybrid phases are stable in a composition range where the Ni-Al chemistry exhibits ambivalence about its preference for either an FCC or a BCC parent crystal structure. It is in this composition range where many orderings are unstable as either FCC or BCC.

The calculated phase diagram of fig. 17 shows that a cluster expansion parameterized with several hundred DFT-PBE formation energies predicts a large Al solubility for γ and a wide concentration range around the stoichiometric $L1_2$ composition of $x_{Ni} = 0.75$ in which γ' is stable. The two-phase region separating γ and γ' is quite narrow, similar to what has been predicted with embedded atom force fields[46] and previous cluster expansions[47]. The phase diagram of fig. 17 also resolves the finite temperature phase boundaries between the family of vacancy rich B2 derived phases. The β phase, having B2-NiAl ordering, accommodates excess Ni as antisite defects on the Al sublattice, but relies on vacancies on the Ni sublattice to achieve Al rich compositions. In the β phase, the vacancies are disordered, however, above a threshold vacancy concentration, the vacancies prefer to order forming distinct phases having ideal stoichiometries of Ni_3Al_4 and Ni_2Al_3. Since these phases have a group/subgroup symmetry relationship with β as a result of vacancy ordering, we have labeled them as β' and β'' respectively.

The β' phase, characterized by a three dimensional arrangement of vacancies (fig. 6c), is considered only in specialized phase diagrams that account for it specifically, such as the one by Ellener and Predel[34]. The β''-Ni_2Al_3 compound appears in most phase diagrams, but is generally not recognized as a derivative structure of B2 NiAl. The calculated phase diagram shows that the vacancy ordering of β''-Ni_2Al_3 is especially stable persisting to temperatures above 1200°C, in contrast to the vacancy ordering of β'-Ni_3Al_4, which disappears through a peritectoid reaction to β'' and β at 840°C. In both β' and β'', the vacancies favor positioning themselves diagonally from each other (fig. 6c and fig. 6b). The common underlying atomic ordering of β, β' and β'' allowed us to calculate their free energies with a single cluster expansion using Monte Carlo simulations.

Two of the δ phases are predicted to be stable in the calculated phase diagram, and because they were modeled as line compounds, they appear as stoichiometric phases. Though some experimentally based diagrams show significant solubility for a Ni_5Al_3 phase (with $\delta_{0^1 2^1}$ ordering), others appear to also indicate line compound behavior, or even omit the phase from consideration completely[35,48]. The high formation energies of antisite defects in $\delta_{0^1 2^1}$ (Ni_5Al_3) suggest that this phase will only be able to accommodate small amounts of configurational entropy, even at high temperatures, providing the basis to model it as a line compound.

An interesting result from the enumerated configurations is the discovery of the many possible low energy δ orderings that appear between $x_{Ni} = 0.625$ and 0.75 (fig. 7). The construction of these orderings by combining $L1_0$ and $L1_2$ layers results in an arbitrary number of configurations that are either groundstates or lie within a couple of meV from the global hull. The existence of these orderings as low energy configurations suggests an alternative mechanism with which a range of compositions around $x_{Ni} = 0.625$ are stabilized that does not require energetically costly antisite defects. Instead of creating antisite defects, an overarching δ phase can instead accommodate an excess of Ni by increasing the ratio of $L1_2$ to $L1_0$ layers, thereby locally preserving their ordering. The high degree of degeneracy among the many possible δ orderings indicate that a range of compositions are likely to be observed experimentally.

Experimental phase diagrams[35] show very high Ni solubility in β, with one assessment reporting a solubility as high as $x_{Ni} \approx 0.65$ at 1200°[35]. Yet, as discussed in III D, a majority of the B2 enumerated configurations (figure 15 b) around $x_{Ni} = 0.65$ are predicted to be dynamically unstable and collapse to an FCC ordering. These zero Kelvin predictions, however, are not necessarily inconsistent with the high temperature experimental observations of a Ni-rich B2 phase. Many high temperature phases, are in fact predicted to be dynamically unstable with DFT at zero Kelvin. Nevertheless, Monte Carlo simulations applied to anharmonic lattice dynamical Hamiltonians have shown that dynamically unstable phases can become stable at high temperature as a result of anharmonic vibrational excitations. TiH_2 and ZrH_2, for example, exhibit a cubic to tetragonal second order structural transition upon cooling[49,50]. The high temperature cubic phases of these hydrides are predicted to be dynamically unstable at zero Kelvin with DFT but become stable at high temperature due to large anharmonic vibrational excitations[17,49,51]. Similar phenomena have been predicted for perovskites[52–55].

A comparison of the strain-energy surfaces of the different groundstates in the Ni-Al binary reveals a strong degree of anharmonicity at compositions where Ni-rich β and the family of δ phases are stable. The strain-energy surfaces of pure Ni, $L1_2$ and stoichiometric B2-NiAl (figs. 9, 10 and 11a) increase rapidly as these crystals are strained. The quasi-harmonic approximation should therefore be sufficiently accurate to account for vibrational excitations in these elastically stiff phases, as was done in past studies[56,57].The shape of the strain-energy surface of $\delta_{0^1 2^1}$, in contrast, is highly anisotropic and shallow (fig. 13b). While the energy minimum of $\delta_{0^1 2^1}$ in e_2-e_3 space is closer to FCC than to BCC, the constant energy contours at energies that are only slightly above the energy minimum in fig. 13b more symmetrically surround ideal BCC than FCC. In fact, the constant energy contours in fig. 13b exhibit shapes very similar to the energy surfaces of TiH_2 and ZrH_2 in e_2-e_3 space, compounds that are tetragonal at low temperature, but transform to cubic symmetry at elevated temperature through a second order structural transition[17,49,51]. This suggests that entropic forces arising from anharmonic vibrational excitations are likely to shift the equilibrium lattice vectors of $\delta_{0^1 2^1}$ away from the energy well close to FCC at low temperature more towards BCC symmetry at elevated temperature. At low temperatures, the system is limited to sampling states close to the global minimum, corresponding to the low symmetry martensite phase. As the temperature is raised, thermal excitations allow the system to sample higher energy states. The anharmonic potential results in an uneven sampling of these high energy states, which shifts the effective symmetry of the austenite phase towards BCC.

The above considerations about $\delta_{0^1 2^1}$ suggest that the BCC symmetry of the Ni-rich β phase is entropically stabilized at high temperature due to large anharmonic vibrational excitations and becomes dynamically unstable at low temperature. This conjecture is consistent with the martensitic transformations exhibited by Ni-rich β upon quenching[7,8,10,58–62]. It also suggests that contributions to the free energy from vibrational excitations are especially important in the free energy description of Ni-rich β, more so than for stoichiometric β NiAl and the other compounds of the Ni-Al binary. Anharmonic vibrational excitations in Ni-rich β are also likely coupled to the local degree of ordering. Describing this coupling will require effective Hamiltonians that are simultaneous functions of displacement degrees of freedom[17,49] and configurational degrees of freedom[25]. Monte Carlo simu-

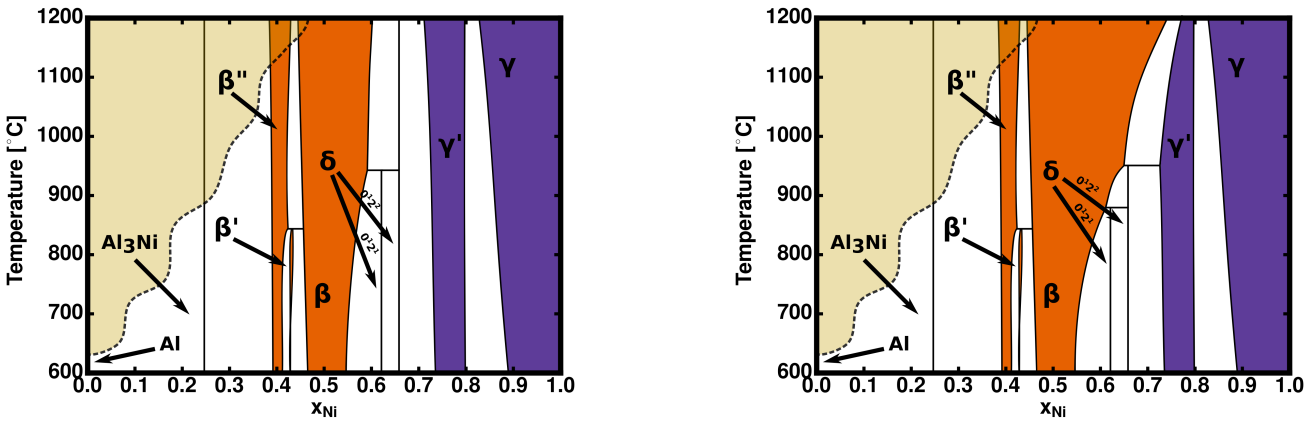

(a) (b)

FIG. 18. Phase diagrams such as fig. 17, with different amounts of artificial vibrational energy contribution added to the β free energies. The vibrational contributions increase with Ni composition and temperature, stabilizing the β (BCC) phase over δ (FCC) orderings.

lations, similar to what was done with EAM potentials[11], will then capture the interplay between anharmonic vibrational excitations, dynamical instabilities and variations in ordering as a function of temperature and reveal the true nature of the martensitic phase transformations that occur upon quenching Ni-rich β. A coupled effective Hamiltonian that combines displacement and configurational degrees of freedom would allow Monte Carlo simulations to predict the onset of the martensitic transformation as a function of temperature and composition. Unfortunately, the construction of such a Hamiltonian currently presents a significant challenge, both for the amount of DFT calculations required as training data, as well as the vast number of resulting basis functions that must be considered in the fit.

While vibrational excitations have not been explicitly addressed in this study, we can speculate as to how their incorporation will qualitatively modify the predicted phase diagram. The importance of anharmonic vibrational excitations in Ni-rich β as compared to that in stoichiometric β (i.e. B2 NiAl), $L1_2$ and the family of δ phases, where vibrations are more harmonic in nature, suggests that Ni-rich β will have more vibrational entropy than the other compounds in the Ni-Al binary. The free energy of Ni-rich β should therefore decrease more than that of the other phases competing for stability upon inclusion of vibrational contributions. Such a lowering of the free energy of Ni-rich β improves the agreement of the calculated phase diagram with experiment. A significant discrepancy between the calculated phase diagram and those published in the literature is the width of the two-phase region separating β and γ'. Experiments show a large Ni solubility in the β phase and a relatively narrow γ' single phase region. The calculated phase diagram, in contrast, predicts a lower Ni solubility in β and a wide stability interval for γ', with the δ phases remaining stable above 1200°C. A lowering of the free energy of Ni-rich β at high temperature will widen the single phase region of the β phase by extending its Ni solubility to higher concentrations, while simultaneously narrowing the composition range of the γ' single phase region. Furthermore, an increased stability of Ni-rich β will decrease the maximum temperature at which the δ phases exist, which is significantly overpredicted in the calculated phase diagram.

We can explore how an increase in the stability of Ni-rich β affects the calculated phase diagram by parametrically modifying the free energy of the β phase. This is shown in fig. 18. The calculated free energy of the β phase above x_{Ni}=0.5 was lowered by subtracting off a term linear in composition and temperature (i.e. the correction term is zero at $x_{Ni} = 0.5$ but grows linearly with excess Ni concentration and temperature). Figure 18 shows that a further stabilization of Ni-rich β relative to the other competing phases increases the Ni-solubility of β, reduces the peritectoid transformation temperatures of the δ phases and decreases the width of the γ' phase. The effect of a doubling of the stabilization is evident upon comparison of fig. 18a and fig. 18b. The phase diagram of fig. 18b closely resembles the reported experimental phase diagrams. The parametric analysis of fig. 18 demonstrates that the additional lowering of the free energy of Ni-rich β relative to the other competing phases yields a phase diagram that is more consistent with experiment than that calculated by considering only configurational degrees of freedom. The strain energy surfaces of section III C suggest that such a lowering of free energy in Ni-rich β should occur due to anharmonic vibrational excitations that are not as important in the other phases.

V. CONCLUSION

We have conducted a first principles study of phase stability in the Ni-Al binary, both at zero Kelvin and at finite temperature. Our results not only confirm the stability of the well charaterized β and γ' intermetallic compounds, but also predict a new family of ground-states derived from β and γ'. A comparison between the calculated phase diagram to experimental data[35,48] shows good agreement with several important discrepancies. The discrepancies considered in conjunction with an analysis of the energy as a function of strain point to the likely importance of anharmonic vibrational excitations in stabilizing the Ni rich β phase at high temperature, which is susceptible to martensitic transformation upon quenching.

VI. ACKNOWLEDGEMENTS

This research was supported by the National Science Foundation (DMR-1105672). Computational resource support was provided by the Center for Scientific Computing at the CNSI and MRL: an NSF MRSEC (DMR-1121053) and NSF CNS-0960316. Crystal structure images were generated using VESTA[63], and plots were generated using matplotlib[64].

* avdv@engineering.ucsb.edu

[1] T. M. Pollock and S. Tin, Journal of propulsion and power **22**, 361 (2006).
[2] T. M. Pollock and A. S. Argon, Acta Metallurgica et Materialia **40**, 1 (1992).
[3] B. Tryon, F. Cao, K. S. Murphy, C. G. Levi, and T. M. Pollock, JoM **58**, 53 (2006).
[4] P. K. Wright and A. G. Evans, Current Opinion in Solid State and Materials Science **4**, 255 (1999).
[5] A. J. Bradley and A. Taylor, Proceedings of the Royal Society of London. Series A, Mathematical and Physical Sciences **159**, 56 (1937).
[6] S. Takizawa, S. Miura, and T. Mohri, Intermetallics **13**, 1137 (2005).
[7] J. L. Smialek and R. F. Hehemann, Metallurgical Transactions **4**, 1571 (1973).
[8] D. Schryvers, L. Toth, Y. Ma, and L. Tanner, Le Journal de Physique IV **5**, C2 (1995).
[9] P. S. Khadkikar, I. E. Locci, K. Vedula, and G. M. Michal, Metallurgical transactions A **24**, 83 (1993).
[10] P. Boullay, D. Schryvers, and J. Ball, Acta Materialia **51**, 1421 (2003).
[11] G. P. Purja Pun and Y. Mishin, Journal of Physics: Condensed Matter **22**, 395403 (2010).
[12] J. P. Perdew, K. Burke, and M. Ernzerhof, Physical review letters **77**, 3865 (1996).
[13] G. Kresse and J. Furthmller, Computational Materials Science **6**, 15 (1996).
[14] G. Kresse and J. Furthmller, Physical Review B **54**, 11169 (1996).
[15] G. Kresse and D. Joubert, Physical Review B **59**, 1758 (1999).
[16] C. Developers, "Casmcode: v0.1.0," (2015).
[17] J. C. Thomas and A. V. d. Ven, Physical Review B **88** (2013), 10.1103/PhysRevB.88.214111.
[18] A. Van der Ven, J. Thomas, Q. Xu, and J. Bhattacharya, Mathematics and Computers in Simulation **80**, 1393 (2010).
[19] B. Puchala and A. Van der Ven, Physical Review B **88** (2013), 10.1103/PhysRevB.88.094108.
[20] C. Wolverton and A. Zunger, Physical Review B **59**, 12165 (1999).
[21] H. Hencky, Zeitschrift fr Physik **55**, 145 (1929).
[22] G. R. Barsch and J. A. Krumhansl, Physical Review Letters **53**, 1069 (1984).
[23] W. Burgers, Physica **1**, 561 (1934).
[24] J. Thomas, A. R. Natarajan, J. Bechtel, and A. Van der Ven, .
[25] J. M. Sanchez, F. Ducastelle, and D. Gratias, Physica A: Statistical Mechanics and its Applications **128**, 334 (1984).
[26] J. M. Sanchez, Physical Review B **81** (2010), 10.1103/PhysRevB.81.224202.
[27] D. de Fontaine, Solid State Physics **47**, 33 (1994).
[28] J. W. D. Connolly and A. R. Williams, Physical Review B **27**, 5169 (1983).
[29] G. L. W. Hart, V. Blum, M. J. Walorski, and A. Zunger, Nature Materials **4**, 391 (2005).
[30] P. A. Korzhavyi, A. V. Ruban, A. Y. Lozovoi, Y. K. Vekilov, I. A. Abrikosov, and B. Johansson, Physical Review B **61**, 6003 (2000).
[31] Y. Mishin, M. J. Mehl, and D. A. Papaconstantopoulos, Physical Review B **65** (2002), 10.1103/PhysRevB.65.224114.
[32] B. Meyer and M. Fhnle, Physical Review B **59**, 6072 (1999).
[33] Q. Xu and A. Van der Ven, Intermetallics **17**, 319 (2009).
[34] M. Ellner, S. Kek, and B. Predel, Journal of Less-Common Metals **154**, 207 (1989).
[35] W. Huang and Y. A. Chang, Intermetallics **6**, 487.
[36] D. de Fontaine, G. Ceder, and M. Asta, Nature **343**, 544 (1990).
[37] A. Van der Ven, M. K. Aydinol, and G. Ceder, Journal of The Electrochemical Society **145**, 2149 (1998).
[38] A. R. Natarajan, E. L. Solomon, B. Puchala, E. A. Marquis, and A. Van der Ven, Acta Materialia **108**, 367 (2016).
[39] Y. Wang, S. Curtarolo, C. Jiang, R. Arroyave, T. Wang, G. Ceder, L.-Q. Chen, and Z.-K. Liu, Calphad **28**, 79 (2004).
[40] P. D. Tepesch, G. D. Garbulsky, and G. Ceder, Physical review letters **74**, 2272 (1995).
[41] B. C. Han, A. Van der Ven, G. Ceder, and B.-J. Hwang, Physical Review B **72** (2005), 10.1103/PhysRevB.72.205409.
[42] Y. Mishin and D. Farkas, Philosophical Magazine A **75**, 169 (1997).
[43] A. Van de Walle and M. Asta, Modelling and Simulation in Materials Science and Engineering **10**, 521 (2002).

[44] A. Van der Ven and G. Ceder, Physical Review Letters **94** (2005), 10.1103/PhysRevLett.94.045901.

[45] A. A. Belak and A. Van der Ven, Physical Review B **91** (2015), 10.1103/PhysRevB.91.224109.

[46] Y. Mishin, Acta Materialia **52**, 1451 (2004).

[47] C. Woodward, A. van de Walle, M. Asta, and D. Trinkle, Acta Materialia **75**, 60 (2014).

[48] I. Ansara, B. Sundman, and P. Willemini, Acta Metallurgica **36**, 997 (1986).

[49] J. C. Thomas and A. Van der Ven, Physical Review B **90** (2014), 10.1103/PhysRevB.90.224105.

[50] R. Quijano, R. de Coss, and D. J. Singh, Physical Review B **80** (2009), 10.1103/PhysRevB.80.184103.

[51] J. Bhattacharya and A. Van der Ven, Acta Materialia **56**, 4226 (2008).

[52] J. C. Wojde, P. Hermet, M. P. Ljungberg, P. Ghosez, and J. iguez, Journal of Physics: Condensed Matter **25**, 305401 (2013).

[53] W. Zhong, D. Vanderbilt, and K. M. Rabe, Physical Review Letters **73**, 1861 (1994).

[54] U. V. Waghmare and K. M. Rabe, Physical Review B **55**, 6161 (1997).

[55] K. M. Rabe and U. V. Waghmare, Physical Review B **52**, 13236 (1995).

[56] R. Arroyave, D. Shin, and Z.-K. Liu, Acta Materialia **53**, 1809 (2005).

[57] A. Van de Walle, G. Ceder, and U. V. Waghmare, Physical review letters **80**, 4911 (1998).

[58] J. H. Maas, L. Toth, A. A. Hamers, and J. Beyer, Le Journal de Physique IV **01**, C4 (1991).

[59] D. Schryvers, Le Journal de Physique IV **5**, C2 (1995).

[60] K. Enami and S. Nenno, Metallurgical and materials Transactions B **2**, 1487 (1971).

[61] S. Chakravorty and C. M. Wayman, Metallurgical transactions A **7**, 555 (1976).

[62] K. Enami, S. Nenno, and K. Shimizu, Transactions of the Japan Institute of Metals **14**, 161 (1973).

[63] K. Momma and F. Izumi, Journal of Applied Crystallography **44**, 1272 (2011).

[64] J. D. Hunter, Computing In Science & Engineering **9**, 90 (2007).